

Empirical overhead of the adapted surface code on defective qubit arrays

Sophia Fuhui Lin¹, Joshua Viszlai¹, Kaitlin N. Smith⁴,
 Gokul Subramanian Ravi¹, Charles Yuan⁵, Frederic T. Chong¹, Benjamin J. Brown^{2,3}

¹University of Chicago

²IBM Quantum, T. J. Watson Research Center, Yorktown Heights, New York 10598, USA

³IBM Denmark, Prøvensvej 1, 2605 Brøndby, Denmark.

⁴Super.tech, a software division of Infleqtion

⁵MIT CSAIL

Abstract

The realization of fault-tolerant quantum computers using solid-state hardware will require us to adapt our quantum error correction (QEC) procedure to account for fabrication variation and defects that will invariably arise. If unaddressed, these errors inhibit us from scaling our system such that quantum information can be processed with sufficiently small failure rates.

We simulate the surface code adapted to defective qubit arrays to find metrics that characterize how defects affect fidelity. We then use our simulations to determine the impact of defects on the resource overhead of realizing a fault-tolerant quantum computer, on a chiplet-based modular architecture. Our QEC simulation adapts the syndrome readout circuit for the surface code to account for an arbitrary distribution of defects. Our simulations show that our strategy for dealing with fabrication defects demonstrates an exponential suppression of logical failure where error rates of non-defective physical qubits are $\sim 0.1\%$ for a circuit-based noise model. This is a typical regime where we imagine running the defect-free surface code. We use our numerical results to establish post-selection criteria for assembling a device with defective chiplets. Using our criteria, we then evaluate the resource overhead in terms of the average number of physical qubits fabricated for a logical qubit to obtain a target logical error rate. We find that an optimal choice of chiplet size, based on the defect rate and target performance, is essential to limiting any additional error correction overhead due to defects. When the optimal chiplet size is chosen, at a defect rate of 1% the resource overhead can be reduced to below 3X and 6X respectively for the two defect models we use, for a wide range of target performance. Without tolerance to defects, the overhead grows exponentially as we increase the number of physical qubits in each logical qubit to achieve better performance, and also grows faster along increase of defect rate. We also determine cutoff fidelity values that help identify whether a qubit should be disabled or kept as part of the error correction code.

1. Introduction

Fault-tolerant (FT) quantum computers will enable the implementation of large-scale quantum algorithms such as

search [30] and factoring [17]. These machines are designed to protect quantum information by encoding logical qubits in quantum error-correcting codes that consist of a large number of interacting physical qubits.

Achieving fault tolerance requires a practical way to manufacture physical qubits. One leading approach is to manufacture a large planar array [11] of qubits in a solid-state system such as superconducting [1, 24, 36] or spin qubits [12, 18]. In these hardware architectures, Ref. [29] estimates that over a million high-fidelity qubits will be required for FT quantum applications.

However, fabricating large-scale solid-state devices for FT applications poses a challenge due to the occurrence of fabrication errors. There are many steps in processing where a slight deviation from the target specification occurs due to process imprecision or stochastically appearing impurities or imperfection [19, 23]. As a result, variation in the quality of qubits as well as the links along which qubits interact is inevitable.

On large-scale devices, physical qubits will exhibit inhomogeneous characteristics, including variations in gate success, measurement fidelity, and coherence, and will likely contain *faulty (defective) qubits* — qubits with severely limited functionality. With today’s technology, [32] estimates that $\sim 2\%$ of the qubits on a transmon device would be faulty.

In this work we numerically assess the logical error rates of the surface code that is adapted to deal with fabrication defects. We then use our simulations to determine the impact of defects on the resource overhead of realizing a fault-tolerant quantum computer, with a modular chiplet architecture similar to [32]. We also study how the overhead is affected by design choices. The surface code is a popular QEC code practical for realization on a chiplet architecture due to its local layout on a two-dimensional grid of qubits. While local connections are sufficient for executing the error detecting ‘stabilizer’ measurements for the surface code, we find a new challenge to realize the surface code in the presence of defects. Specifically, we cannot measure certain stabilizers in the vicinity of a defect and, as such, some errors may go undetected.

We can realize an adapted surface code on a defective chiplet by making ‘super-stabilizer measurements’ that can identify errors near to defective regions [2, 33–35]. We illus-

trate the construction of super-stabilizers in Fig. 1. Conveniently, we can measure super-stabilizers using the non-faulty qubits close to the defective region [2, 33, 34], and in a timely manner. Furthermore, it has been shown, in theory, that this approach can scale on a large lattice [35]. However, no previous work has been conducted to determine the performance of any such adapted protocol relative to the defect-free surface code, or the overhead it incurs. This is essential to determine the practicality of dealing with fabrication defects using this method. To conduct our numerical simulations we develop an automated method to map surface code to defective grids by deforming boundaries and forming super-stabilizers. Notably, our automated method can define a surface code for an arbitrary configuration of defects.

Using our numerical results, we identify two key figures of merit that characterize the fidelity of a surface code on a defective chiplet. The first is the distance on the defective patch d , the least number of physical errors that can lead to a logical failure. In the regime of low error rate per gate, p , we find that to leading order, the logical failure rate decays like $O(p^{d/2})$, just as for defect-free chiplets. Remarkably, we identify this scaling when physical errors occur at a rate $p \sim 10^{-3}$, the regime where we expect a defect-free chip to be operable. This implies that the defective chips are functionally similar to the defect-free ones with the same d , except that they cost more physical qubits. Aside from this scaling, we identify variation in surface codes with equivalent code distances. We find a second figure of merit that differentiates among these codes. Specifically, we find that the logical failure rate will scale with the number of different ways that a logical failure can occur with d physical errors. Both of these figures of merit can be efficiently computed after the surface code is adapted to a defective grid.

These two indicators enable us to rapidly assess the quality of individual defective chiplets. This is necessary for establishing a post-selection criterion for the modular chiplet architecture, and also for resource overhead evaluation. The modular architecture is more flexible than a monolithic one because it allows the post-selection of chiplets before connecting them into a larger device. Exploiting this flexibility helps reduce the cost of fabrication, but in our setting it requires an informed post-selection criterion that accounts for how each chiplet is affected by the defects on it. This is different from the setting in [32], where the goal is to assemble a defect-free chip. Our numerical results demonstrate that our post-selection criterion is more effective than the natural strategy to select the chiplets with the fewest defects.

We quantify the resource overhead by the total number of fabricated physical qubits per logical qubit, including the qubits on the chiplets that are not selected. In Fig. 12b, 13b, and 17b we show the factor of resource overhead relative to the ideal no-defect case. Our results show that it is important to select the chiplet size based on the fabrication error rate, in order to achieve a balance between having a high yield

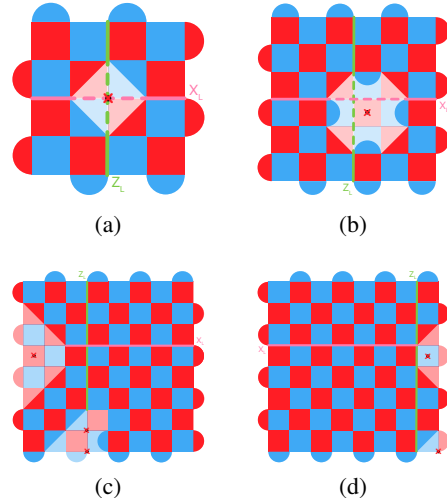


Figure 1: Examples of super-stabilizers and boundary deformations. The faulty qubits are marked with a red 'x', and the excluded part in a patch is represented by lighter color. (a) One broken data qubit in the interior, handled by a super-stabilizer. (b) One broken syndrome qubit in the interior, handled by larger super-stabilizers. (c)(d) Broken qubits near the boundary require boundary deformations.

(proportion of chiplets that meet the standard) and using a small number of physical qubits per patch of code. When the optimal chiplet size is chosen based on the results, the resource overhead is below 3X and 6X respectively for the two defect models we study (defective links only v.s. same rate of defect on links and qubits), when the defect rate is below 1%. This holds for a wide range of performance targets. Without the ability to tolerate defects, the resource overhead grows exponentially with the number of physical qubits in a logical qubit (which increases for higher performance targets) and also grows faster with the defect rate.

We also evaluate the sensitivity of the yield to two design choices: what boundary constraint is imposed on each patch, and whether the chiplet design allows the data and syndrome qubits to be swapped by rotating a chiplet. Although in this paper we mainly evaluate each patch by its capacity to store a logical qubit, a boundary constraint can ensure the quality of multi-qubit logical gates.

Finally, we identify cutoff fidelity values for determining whether a qubit should be treated as faulty or kept in the code. This is important in the practical setting because the impact of fabrication errors varies and there's not always a clear line between faulty and good qubits.

1.1. Summary of contributions and results

- We develop an automated method that adapts the rotated surface code to a grid with an arbitrary distribution of defects using super-stabilizers. Our automated method produces a simulation of active error correction that is implemented on stim [14].
- Using our numerical simulations we identify effective indi-

cators for assessing the fidelity of surface code adapted to defective chiplets.

- We present the first evaluation of the impact of fabrication defects on the quantum error correction resource overhead. Our focus is on the modular chiplet architecture where one logical qubit is allocated on each chiplet. We quantify the resource overhead with the average number of physical qubits fabricated for a logical qubit, and evaluate its sensitivity to system parameters. We show that the post-selection of chiplets and the ability to use defective chips are both critical for reducing the extra overhead due to fabrication errors.
- We identify cutoff fidelity values for determining whether a qubit with worse performance than its neighbors should be treated as faulty or kept in the code.

2. Background

2.1. Fabrication errors and variations on transmon-based quantum devices

In this section, we discuss some of the sources of fabrication errors and variation for transmon qubits. Although our discussion is not exhaustive, it is meant to give some intuition for why current chips see a 2% defect rate.

Imprecision in the fabrication of Josephson Junctions (JJs) is a source of varied qubit performance. A JJ, two superconductors separated by a thin metal-oxide insulator, is the heart of a transmon qubit [13]. JJs have incredibly small feature sizes that are hundreds of nanometers in scale [19], smaller than the wavelengths used during optical lithography. Thus, slight imperfections that appear in JJ positioning, component dimension, or surrounding layers influence operational characteristics of the transmon [23].

On fixed-frequency transmons with fixed couplers, one of the most commonly used superconducting qubits, frequency collision is a dominant type of fabrication error. Fabrication variation can deviate a qubit's frequency from its ideal, resulting in spectral overlaps that cause frequency collisions. This variation is stochastic, causing the resulting frequency profile of each chip to be unique.

Another type of unintended defect that frequently and stochastically appears across a quantum chip during processing is a two-level system (TLS) [27]. A TLS is caused by impurities inside materials or irregularities within atomic crystalline lattice structures appearing unexpectedly in oxide layers or on the surface of the chip. Because of the layered approach associated with transmon processing, there are many opportunities for TLSs to appear during fabrication.

2.2. Surface code

The surface code [9, 11, 22] is among the most practical quantum error-correcting code for physical realisation due to its implementation using a two-dimensional nearest-neighbour qubit layout, and its high tolerance to noise. It can perform a universal set of logic gates while maintaining its local pla-

nar layout using lattice surgery to perform entangling operations [8, 21, 25] and magic state distillation [5, 16] to perform non-Clifford gates. For the most part of this work we will concentrate on the performance of the surface code storing a logical qubit over time. In this paper, we use the rotated planar surface code due to its low qubit overhead [3, 4, 10]. We define the surface code with code distance d on a $d \times d$ grid of data qubits. The errors on the data qubits are detected using $d^2 - 1$ measurement qubits, otherwise known as ancilla qubits or syndrome qubits. More specifically, a measurement qubit is placed on either a red or a blue face of the grid of data qubits, see Fig. 2. Note also that the faces at the lattice boundary each touch two data qubits.

We measure stabilizers to detect errors that qubits experience. Stabilizers are measured repeatedly in cycles to determine the locations of errors that occur over time. In each cycle, each measurement qubit is used to measure either a Pauli-X stabilizer, $\hat{X}_a\hat{X}_b\hat{X}_c\hat{X}_d$, or a Pauli-Z stabilizer $\hat{Z}_a\hat{Z}_b\hat{Z}_c\hat{Z}_d$, depending on the color of the lattice face on which the measurement qubit lies. The measurement qubits on the boundary only acts on two data qubits, and therefore measure stabilizers of the type $\hat{X}_a\hat{X}_b$ or $\hat{Z}_a\hat{Z}_b$. Stabilizers are measured with circuits that are detailed in, e.g., Ref. [38].

In practice, to deal with the errors that occur on data qubits, as well as errors that occur on measurement qubits that may cause stabilizer circuits to give unreliable outcomes, we compare a stabilizer reading at cycle t to the reading of the same stabilizer made at cycle $t - 1$. A difference in reading gives rise to an error detection event.

By performing many cycles we obtain a large history of detection events over time, that we call the error syndrome. In general, we can regard errors as string-like objects in this error syndrome, where detection events occur at the end-points of these strings. See, e.g. Refs. [7, 9, 11, 39] for details. Using the error syndrome, we can obtain a correction to recover encoded information using minimum-weight perfect-matching algorithm [7, 9, 11, 20, 39], where we deal with detection events due to Pauli-X stabilizers and Pauli-Z stabilizers separately. We concentrate on only Pauli-Z stabilizers throughout this work, but note that an equivalent analysis will hold for the alternative stabilizers.

A logical error is introduced to the surface code when at least $d/2$ errors occur along a non-trivial path over the surface code error syndrome history [3, 9, 11, 39]. If we assume that an individual error occurs with probability $O(p)$, then in the limit that p is small, we can fit the logical error rate to the ansatz

$$LER = \beta(Np)^{\alpha d}, \quad (1)$$

where N and $\alpha \leq 1/2$ are constants to be determined [3, 6, 9, 11, 39, 40].

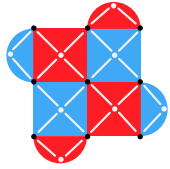


Figure 2: Rotated surface code with $d=3$. The black dots represent the data qubits, and each red (blue) face represents an X (Z) stabilizer. Each stabilizer requires an ancilla qubit.

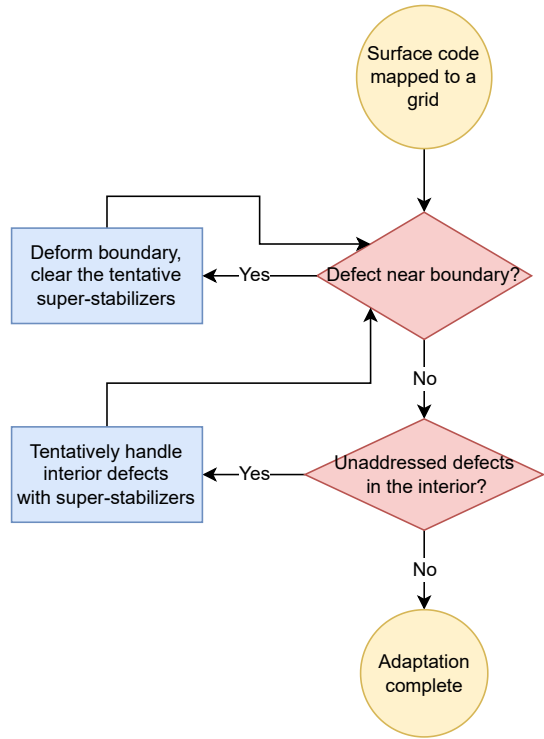


Figure 3: Algorithm for mapping rotated surface code to a defective grid by deforming boundaries and forming super-stabilizers.

3. Deforming boundary and forming superstabilizers

Faulty qubits and links can be particularly harmful to the implementation of topological QEC codes if they are not handled correctly. This is because qubit errors in the vicinity of fabrication defects may not be detected. Given a finite density of fabrication defects, this will inhibit the decay of logical failure rate as we increase code distance, if we do not deal with these defects correctly.

Building upon the theory in Ref. [35], we develop and implement an automated method that adjusts surface code for arbitrary defect distributions. Our algorithm includes deforming boundaries of a code and forming super-stabilizers in the interior. A flowchart is shown in Fig. 3. Our code takes the chiplet size and a list of defects as input, then adapts surface code to the defective grid and generates a stabilizer measurement circuit compatible with the Stim [14] simulator.

We learn the occurrence of errors close to fabrication de-

fects by forming super-stabilizers around them. The values of these super-stabilizers can be inferred from local measurements around the defects [2, 33, 34]. Furthermore, we repeat the local measurements used to obtain the superstabilizer for an elongated time, over a timescale that is commensurate with the size of the superstabilizer that defect [35]. A measurement schedule with this feature is adopted in Ref. [35] to demonstrate the procedure helps achieve a threshold - when the physical errors on the non-faulty qubits is lower than the threshold, one can expect the quality of the logical qubit to improve as we encode it with more physical qubits.

As an example we show how we can construct a weight-6 X and Z super-stabilizer about a single faulty qubit in the interior of the code in Fig. 1a). The value of the X (Z) super-stabilizer can be computed from the direct product of the two weight-3 broken X (Z) stabilizers used as gauge operators. The X and Z gauges anti-commute, so they cannot be measured in the same cycle. Instead they are measured in alternate cycles.

Another important example is the case where a measurement qubit in the interior of the qubit grid is faulty (Fig. 1b). All of its neighbouring data qubits are disabled and larger super-stabilizers (each consisting of 4 gauge operators) are formed. Around a larger defect cluster like this, instead of measuring the X and Z gauges in alternate cycles (XZ...), we repeat one type of measurement several times before switching to the other (e.g. XXZZ...) following [31, 35]. The number of repetitions should scale with the size of the cluster [31, 35]; here we set the number of repetitions equal to the diameter of the defect cluster.

Note that when forming super-stabilizers in the interior, we not only need to disable the data qubits connected to defective syndrome qubits, but also need to disable syndrome qubits due to defective data qubits in some cases. It is obvious that a syndrome qubit connected to no more than one active data qubit needs to be disabled. When a syndrome qubit is connected to two active data qubits but the three qubits are on the same diagonal line, it also needs to be disabled.

If a faulty qubit is too close to the boundary to be surrounded by gauge operators, it cannot be handled by super-stabilizers. In this case the boundary of the patch needs to be deformed to exclude the faulty qubit. Although [2] addressed the boundary deformation for a surface code with a different lattice geometry, the rotated surface code has more complicated boundaries and we develop a new algorithm for handling the defects near boundary.

To illustrate a boundary deformation, four examples are shown in Fig. 1 (c) and (d). On the right side of (d) is a faulty syndrome qubit near a boundary of different color. Two data qubits are disabled along with it, because they are no longer included in any Z stabilizer. Then the X syndrome qubit on its right is also disabled, because it no longer has any data qubits to measure. If any of these three qubits were the faulty one, the same boundary deformation would apply. If a faulty syndrome qubit is near a boundary of the same color, as is the

case on the left of (c), more qubits need to be excluded from the patch to ensure that all stabilizers on the boundary are of the same color. In particular, the neighboring syndrome qubits of different type than the boundary need to be excluded from the patch. If a data or syndrome qubit at a corner is faulty, then only one other qubit needs to be excluded (lower right of (d)). If any faulty qubit is too close to the new boundary, it must be excluded too. To the lower left of (c) such an example is shown. The faulty data qubit on the original boundary leads to an excluded region that is similar to the one on the right edge of (d). Then since a data qubit on the new boundary is faulty, the lower boundary is further deformed. Note that the second faulty qubit in this region was part of three stabilizers that remained active after the first deformation, but only the one of different color than the lower boundary is excluded in the second deformation.

The code distance d is the length of the shortest undetectable error chain on a patch of QEC code, and is equivalent to the length of the shortest X or Z logical operator. As we will show in Sec. 4, it not only characterizes the defect-free codes, but also serves as a primary indicator for the fidelity of defective patches. On a $l \times l$ patch, we have $d = l$ only if there's no defect; a defective patch has $d < l$. In Fig. 1 (a), $l = 5$ and $d = 4$ along both directions. In (b), we have $l = 7$ and $d = 5$. In (c) and (d) $l = 9$. The code distance is 7 in (c). In (d) the distance is different along each direction: $d = 9$ vertically and $d = 8$ horizontally.

4. Building a device with defective qubits

In this section we move on to the setting where the goal is to build a large FT device with an array of rotated surface code patches. We first propose a modular architecture and discuss design choices, then identify a post-selection criterion for evaluating the quality of defective chiplets, and finally show the resource overhead and a sensitivity analysis.

For the simulation we use two models of fabrication errors: one with links set to be faulty at random, and one with links and qubits both set to be faulty at the same probability. The first one models fixed-frequency transmon qubits with fixed couplers, where frequency collision is the dominant type of fabrication error. The latter models tunable transmon qubits, where links are as intricate as qubits. When using the super-stabilizers, a faulty link can be handled by disabling either of the two qubits that it connects. Faulty syndrome qubits lead to greater damage as explained in the last section, so we choose to disable the data qubit connected to a faulty link unless the syndrome qubit on the other end is already disabled.

We use a circuit-level noise model for the physical errors on the non-defective qubits, where the two-qubit gate error is p , the one-qubit gate error is $0.8p$, and the readout error is $\frac{8}{15}p$. We use standard measurement circuits for the syndromes [38].

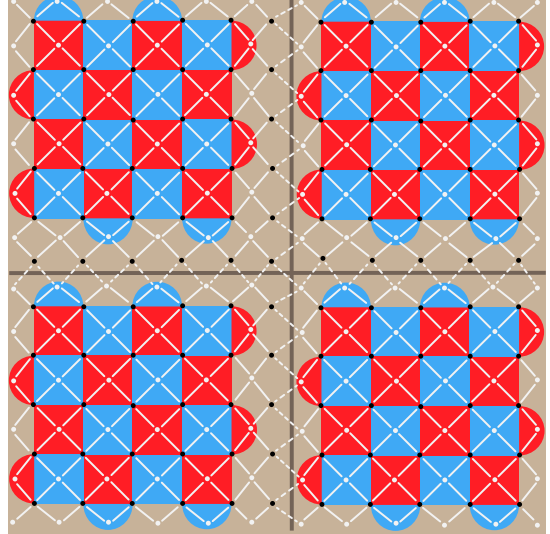


Figure 4: Schematic of a chiplet architecture.

4.1. A modular architecture for rotated surface code

The modular architecture we simulate in this project is an array of chiplets similar to the ones in [32]. We allocate one patch of surface code on each chiplet, as in Fig. 4. The qubits on adjacent chiplets can communicate via the inter-chip links (shown in dashed lines), but these links are currently $\sim 3X$ worse than on-chip links [32]. Since no patch is defined across multiple chiplets, the inter-chip links are not used when a patch is idle. We assume the physical qubits on each chiplet has the grid connectivity, which is the one that naturally supports surface code.

In Fig. 4 we show a design that allows one to swap the assignment of the data and syndrome qubits on a chiplet by rotating the chiplet by 180° . When a chiplet contains more faulty syndrome qubits than faulty data qubits, this will likely improve the quality of the code, because faulty syndrome qubits generally cause more significant drop in fidelity. In Sec. 4.3 we will evaluate how much advantage this degree of freedom translates to.

4.2. Post-selection criterion: assessing the quality of defective chiplets

When building a modular device, one has the opportunity to select the chips with better quality, and arrange them in a way that maximizes the fidelity. In [32], only the defect-free chiplets are kept, and then they are combined in a way that avoids frequency collisions along inter-chip links. When the goal is to support the surface code, we need different post-selection criteria. The chiplets that support higher-quality surface code patches should be kept, and they should be arranged to ensure that they can communicate at full code distance via lattice surgery.

For the purpose of selecting and arranging chiplets, we need to find good indicators for the ability of a defective chip to

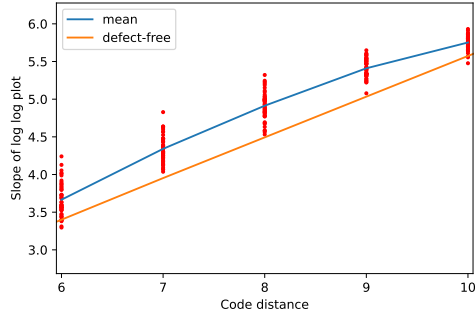


Figure 5: Slopes of the log-log LER v.s. p plots, from randomly sampled defective rotated surface code patches with $l = 11$. For each value of d , 50 defective patches are sampled, with the same probability for link failure and qubit failure.

support a good surface code encoding and lattice surgery. This is because in a realistic setting, it might be impractical to experimentally measure the fidelity of surface code patches encoded on each chiplet before deciding which ones to use. Experimentally testing the fidelity of lattice surgery operations between patches on different chips is even less practical, since it requires repeatedly connecting and disconnecting chiplets to iterate through different combinations. When the target logical error rate (LER) is tiny, the cost of running simulations (e.g. a memory experiment) to estimate fidelity is also formidable. This is because when the LER is small, it takes too many shots to observe enough instances of logical errors.

To investigate the relevance of different figures of merit for many sample chiplets, we need a way of evaluating the quality of individual chiplets. We adopt Eqn. (1) to devise one such quantity. Specifically, we look to find the exponent αd of this expression. To obtain this number, for each sample chiplet, we evaluate the logical failure rate as a function of p for values of $5 \times 10^{-4} \leq p \leq 2 \times 10^{-3}$ where logical failure rates are determined using Monte Carlo methods. This is a typical regime where the defect free surface code is studied [11]. The value αd is the gradient of the logical failure rate shown as a function of p plotted with logarithmic axes. As such we will refer to this value as ‘the slope’. We show logical failure rates plotted as a function of p in Fig. 6. The straight lines given in the plot indicate that we are sampling in a low p regime where Eqn. (1) is valid.

We explored various possible indicators including d of the defective patches, the total number of qubits that get disabled (a quantity that is generally higher than the number of faulty qubits), the size of the largest cluster of disabled qubits. The code distance of a defective surface code patch is the best indicator we find (Fig. 5). Although [2] suggests that defective patches are outperformed by defect-free patches with the d , their data (Fig. 14 in [2]) only supports this claim for physical error rates $\geq 3 \times 10^{-3}$. Instead, we find that the defective patches generally have higher slopes than the defect-free patches with the same d (Fig. 5). This means although the

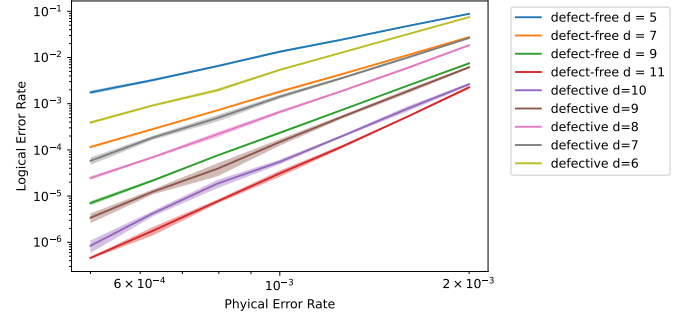


Figure 6: Logical error rate v.s. physical error rate at low physical error rates (5×10^{-4} to 2×10^{-3}), for defect-free patches of rotated surface code, and examples of defective patches with $l = 11$. The shaded regions represent the 95% confidence intervals for each value.

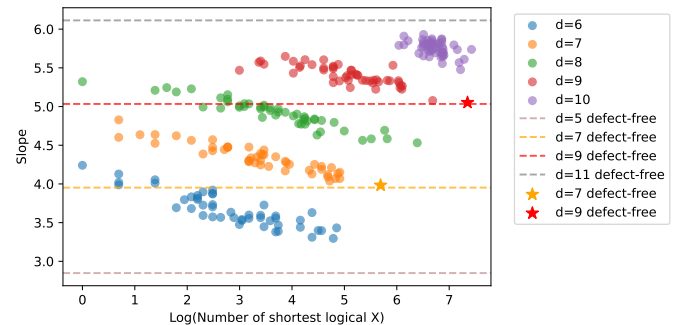


Figure 7: Slopes of LER v.s. p , from the same defective patches used in Fig. 5, grouped by d and plotted against the log of the number of shortest logical X .

defective patches perform worse than the defect-free counterparts at higher p , they generally perform better at lower p .

To explain the variation among patches with the same d , we identified a secondary indicator, the number of unique weight d logical operators. In other words, it is the number of different ways that a logical failure can occur with d physical errors. It can be evaluated efficiently with a modified version of breadth-first search on a graph where the nodes are the physical qubits on a surface code. As shown in Fig. 7, this helps to identify the outliers that significantly outperforms or under-performs compared to the defective patches with the same d . This indicator also helps us to understand why defective patches generally outperform defect-free counterparts with the same d : a defect-free patch has more symmetry in its shape so it has a large number of unique minimum-weight logical operators.

In Fig. 8 and 9 we evaluate two other indicators that we tested. The size of the largest defect cluster does not help predict the slope. The proportion of disabled data qubits is inversely correlated with the slope, but does not provide extra information that one cannot tell from the d .

Now we compare our post-selection criterion against a baseline indicator, the number of faulty qubits on a chiplet. Although there is a visible negative correlation between this

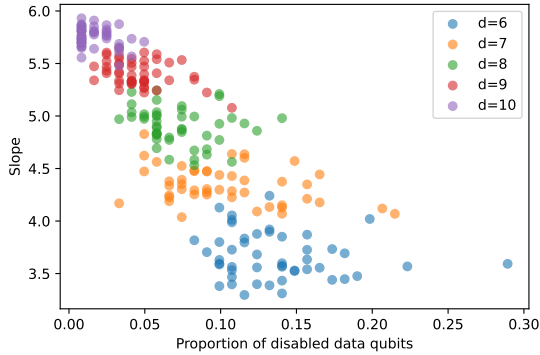


Figure 8: Slopes of LER v.s. p , from the same defective patches used in Fig. 5, grouped by d and plotted against the proportion of disabled physical qubits on a patch.

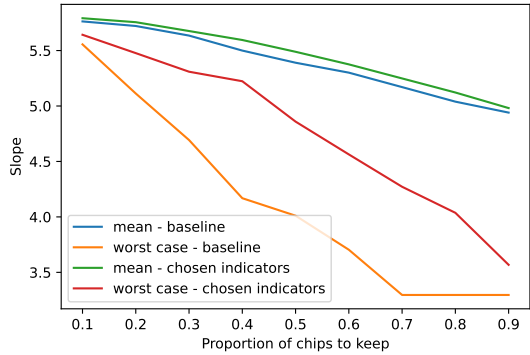


Figure 11: Mean and worst slopes of selected patches, when the proportion selected is varied. The baseline only uses the number of faulty qubits (Fig. 10); the “chosen indicators” use d as primary indicator and the number of shortest logical operators to break ties.

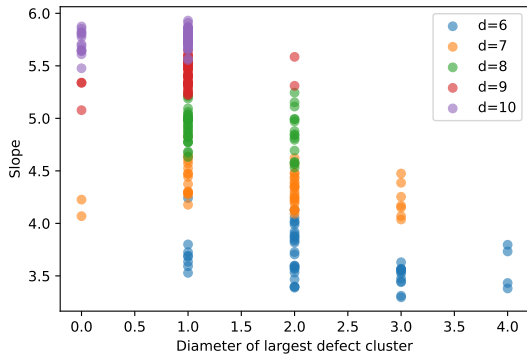


Figure 9: Slopes of LER v.s. p , from the same defective patches used in Fig. 5, grouped by d and plotted against the diameter of largest cluster of disabled qubits.

quantity and the slope in Fig. 10, it is not as effective as the indicators we choose in Fig. 11.

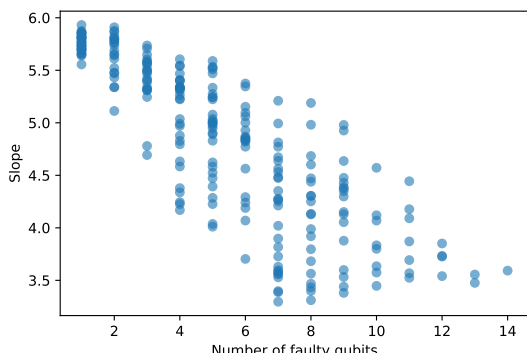


Figure 10: Slopes of LER v.s. p , from the same defective patches used in Fig. 5, plotted against the number of faulty qubits on a patch.

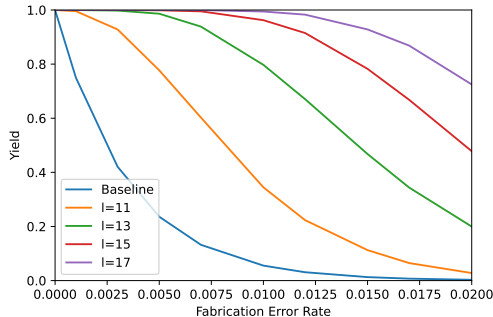
4.3. Resource overhead and sensitivity analysis

In this section we show how fabrication errors increase the resource overhead of the surface code, and show that a modular architecture design and the ability to adjust.

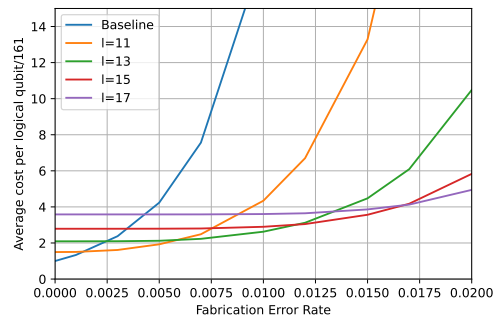
When the goal is to match the fidelity of the $d = 9$ defect-free patch, we have the choice of using chiplets of width 9, 11, or larger. What chiplet size is more resource-efficient? If we make larger chiplets, each patch has a higher l . Then under the same fabrication error rate we expect more chiplets to meet the standard. With smaller chiplets we have a lower yield, and for the baseline where $l = 9$, we cannot tolerate any defects. But each larger chiplet is made with more resources, which we quantify as the number of physical qubits. In Fig. 12(a) we show the yields and in (b) we show the average number of fabricated physical qubits for a logical qubit, which is obtained by dividing the number of qubits on each patch by the yield. The simulation is run with the model that only has faulty links, and each data point is collected from a 10000-shot simulation. From Fig. 12(b) we can tell that below a fabrication error rate of $\sim 0.1\%$, we should choose the baseline. From $\sim 0.1\%$ to $\sim 0.6\%$ and from $\sim 0.6\%$ to $\sim 1.1\%$, we should choose $l = 11$ and 13 respectively. When the fabrication error rate is above $\sim 1.1\%$, we should choose $l = 15$ or higher. The overhead factor of the baseline approach rises out of the figure at higher defect rates. It is 18X and 336X respectively at 1% and 2% defect rates.

When we use the model where links and qubits have the same defect rate (Fig. 13, instead of the link-defect-only model, the yields are lower than in Fig. 12 and the advantage of using larger l start from a lower defect rate. At a 1% defect rate, the overhead factor of the baseline approach ($l = 9$) is 91X.

For most of the paper we focus on the fidelity of an individual patch. Here we briefly discuss how certain deformations on the boundary would result in a drop in code distance during lattice surgery, and evaluate the cost of avoiding such chiplets.



(a)



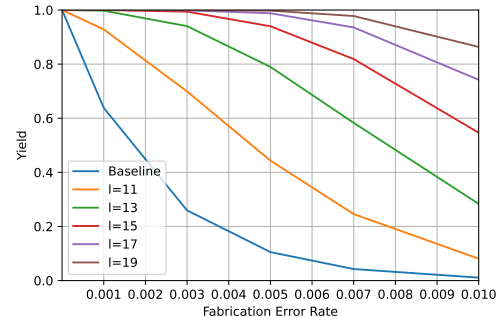
(b)

Figure 12: Defective links only. (a) Proportion of chiplets that support a rotated surface code patch that performs as well as a defect-free patch of distance 9, evaluated with the two metrics in 7. (b) As for (a) but showing the average number of fabricated physical qubits per logical qubit scaled by the number in the no-defect case.

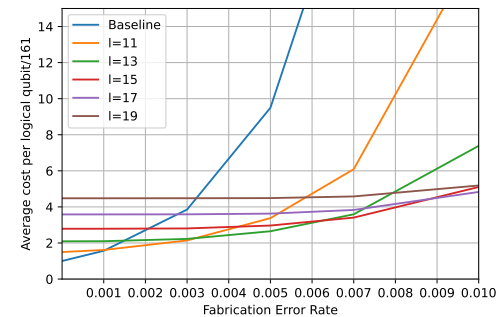
Lattice surgery involves merges and splits between patches of planar surface code. In Fig. 14 we show an example case where a deformed boundary only leads to a small decrease in the distance of the individual patch, but causes a larger decrease of code distance after a merge. In this example the two merging edges are deformed at the same place. When the deformations are not aligned, there can be a greater drop in code distance after the merge. A low-distance merge has lower fidelity, so when this type of patch is used, the compiler should try to schedule lattice surgery operations on its other edges. Then the programs would be compiled to more layers. Alternatively, one can avoid using patches with such an edge, which may result in a lower yield.

Note that we did not run simulation to compute the fidelity of lattice surgery operations between defective patches. Therefore it is only our speculation that the code distance of the merged patch is sufficient to predict the fidelity of the logical operations.

In Fig. 15 we show how the yield changes after a boundary constraint is imposed. We have two types of boundary constraints for an edge of a surface code patch: (a) free of deformations (in this case we don't need to form any new



(a)



(b)

Figure 13: Links and qubits are assigned faulty at the same rate. (a) Proportion of chiplets that support a rotated surface code patch that performs as well as a defect-free patch of distance 9, evaluated with the two metrics in 7. (b) As for (a) but showing the average number of fabricated physical qubits per logical qubit scaled by the number in the no-defect case.

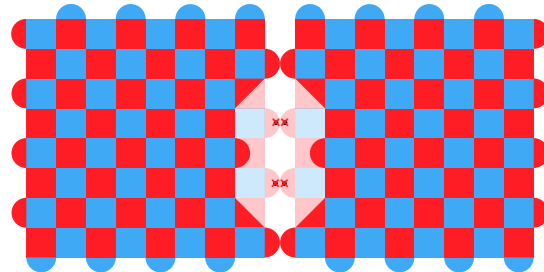


Figure 14: An example where the code distance drops after a merge.

super-stabilizer during lattice surgery) (b) the total width of deformations along the edge is not enough to decrease the code distance after a merge. Then we have the choice of imposing the constraint on (c) all four edges of a patch, or (d) on only two edges (at least one X-edge and at least one Z-edge, for the convenience of scheduling lattice surgery operations). From these we get four different boundary constraints. The yield drops significantly only when we impose the strictest constraint (standard 1, or a and c). The drop is negligible for standard 4, when we impose (b) and (d). And when we impose standard 2 or 3, the drop is visible but small. Given

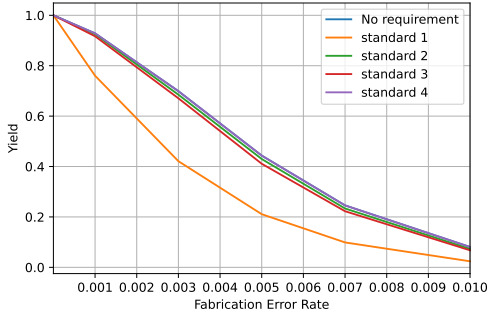


Figure 15: The change in yield after imposing different standards on boundaries of patches. Standard 1: No deformation on any boundary; standard 2: at least 2 boundaries of different types have no deformation; standard 3: all 4 boundaries support lattice surgery without decreasing distance; standard 4: at least 2 boundaries of different types support lattice surgery without decreasing distance.

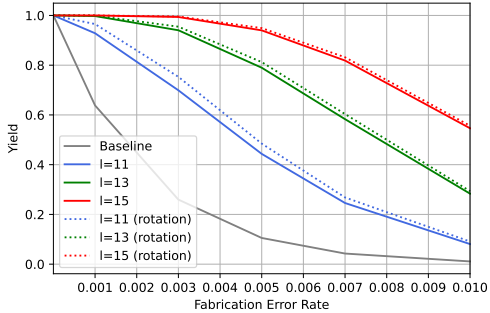
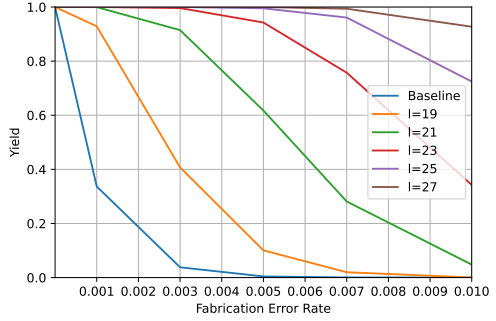


Figure 16: Improvement in yield when there is freedom to rotate the chiplets. Links and qubits are assigned faulty at the same rate.

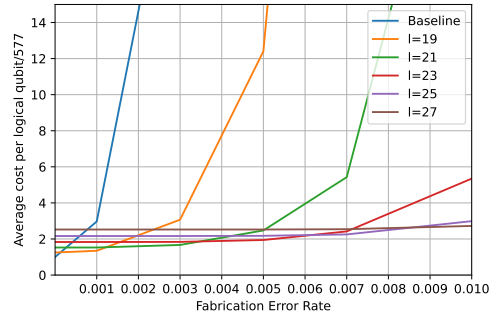
the results, we should apply standard 3 if we are willing to form new super-stabilizers along the merging/splitting edges; if not, we should apply standard 2.

The way we propose to allocate a surface code patch on a chiplet (in Sec 4.1) allows the freedom to swap the assignment of data/syndrome qubits by a 180° rotation. We observe a small improvement in yield when we have such a freedom (Fig. 16). The improvement is smaller in the regime with a higher number of faulty qubits - when l is large or the fabrication error rate is high. This is because when there are defects on both links and qubits, a patch tends to have more faulty data qubits than syndrome qubits since we handle each defective link by disabling the end with data qubit. And this holds with a higher certainty when there are more defects. Some techniques to reduce leakage errors involve swapping data and ancilla qubits [26], which might not work well with this design. Handling leakage errors is outside the scope of this paper though.

In Fig. 17 we show the cost of making higher quality logical qubits. For this set of simulations, instead of matching the fidelity of the $d = 9$ defect-free rotated surface code, the goal is to match the $d = 17$ defect-free code. The trends we observe



(a)



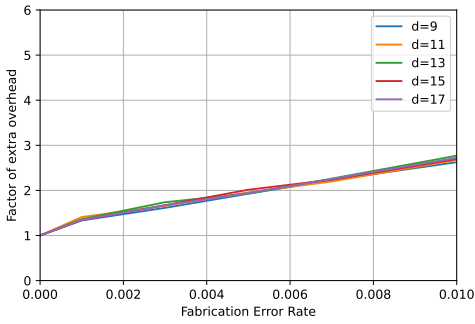
(b)

Figure 17: Yields for larger chiplets. Defective links only. (a) Proportion of chiplets that support a rotated surface code patch that performs as well as a defect-free patch of distance 17, evaluated with the two metrics in 7. (b) As for (a) but showing the average number of fabricated physical qubits per logical qubit scaled by the number in the no-defect case.

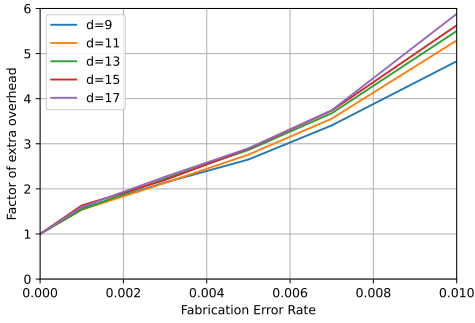
are qualitatively the same. Note that at 1% defect rate, the factor of resource overhead from the $l = 17$ defect-intolerant baseline is over 56000X. In fact, when the defect rate is fixed, the resource overhead increases exponentially with the number of physical qubits in a logical qubit.

On Fig. 12b, 13b, and 17b, if we take the minimum of all curves at each fabrication error rate, we obtain the minimum extra resource overhead (due to defects) that can be achieved by the chiplet architecture considered in this work. In Fig. 18 we show how this factor is affected by the fabrication error rate and the target code fidelity. When the fabrication error model consists of defective links only, the curves for different target fidelity coincide. It is $\sim 2X$ at a 0.5% defect rate, and below 3X at 1% defect rate. When we model both defective qubits and links, the curves coincide at low defect rate and diverge a small amount at higher defect rate. The factor of overhead is $\sim 3X$ at a 0.5% defect rate and 5X to 6X at 1% for the range of fidelity targets we set.

Fig. 18 shows that, even with a method to implement QEC in the presence of fabrication errors, it is still important to reduce the defect rate by adopting improved designs for qubits



(a) Defective links only.



(b) Defective links and qubits.

Figure 18: The extra resource overhead due to defects, for different target logical error rates. The y-axis is the average number of fabricated qubits for a logical qubit, scaled by the number in the ideal no-defect case. The target logical error rate is the fidelity of the defect-free rotated surface code of code distance d .

or fabrication. Limiting the factor of overhead to below 2X requires a defect rate below $\sim 0.5\%$ for the link-defect only model, and below $\sim 0.2\%$ for the model with both defective links and qubits.

4.4. Limit of the monolithic architecture

The results in Sec.4.3 demonstrates that the ability to implement the surface code on defective grids is necessary for containing the resource overhead, by comparing against a baseline design that uses modular chiplets but only accepts defect-free surface code patches. What if we choose a monolithic architecture but accept defective patches?

On a monolithic device holding an array of surface code patches, not all the good patches can be used - they must also be connected at the very least. In Fig.19, we show the results from simulating a monolithic device holding a square array of logical qubits. Each patch of logical qubit is randomly assigned to be good/bad, then we search for the largest connected component (LCC) of the good patches. The x-axis of the figure is the total number of patches on the device, while the y-axis shows the expected size of the LCC of good patches and the expected number of good patches. The results

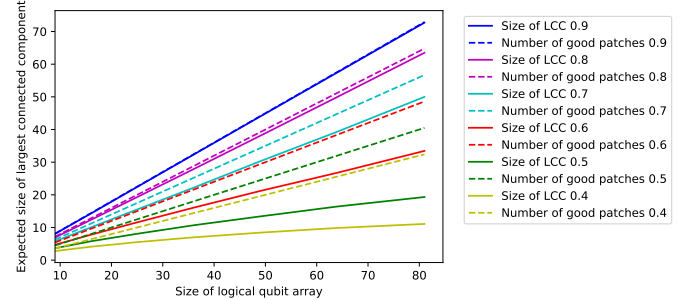


Figure 19: Limit of a monolithic architecture. The figure shows the expected size of largest connected component of the good patches on a square array of surface code patches allocated on a monolithic device, where each patch is randomly assigned to be good/bad. The label of each line is the proportion of the good patches.

show that not all the good patches on a monolithic device are connected unless the yield is as high as 90%.

We conclude that the monolithic architecture imposes a higher requirement on the yield. A very high proportion of the patches must be good, otherwise the good patches are disconnected by the bad ones. For example, in the setting of Fig.13, the yields from the most resource efficient approaches are 63.7%, 69.9%, 79.0%, 81.9%, and 74.2% respectively at defect rates 0.1%, 0.3%, 0.5%, 0.7% and 1%. In all 5 cases some of the good patches will be disconnected. When the yield is 63.7%, on a device with 10 by 10 patches the expected size of the LCC is 48.3, which means 24% of the good patches (63.7) are not in the LCC. Note that evaluating the size of LCC of good patches on a monolithic device does not fully reflect the disadvantage of the monolithic architecture. Most importantly, the good patches in the same connected component on a monolithic device are connected more sparsely than those on a modular device solely made with good patches. Furthermore, the modular design provides the flexibility to reduce the poor match of edges that may result in low-quality lattice surgery. This optimization is not available on a monolithic architecture.

5. What counts as a fabrication error

So far we have been using a simple model for defects, where each qubit or link is labeled directly as “faulty” or “non-faulty”. In real life, there are scenarios where it is not clear whether a qubit should be viewed as faulty. For example, on a device with a average 2-qubit gate fidelity of 99.9%, should we disable a qubit that only supports 2-qubit gates with 97% fidelity? If the cutoff is set too high, we lose too many physical qubits and suffer a decrease in code performance; if the cutoff is too low, the inferior qubits will also damage the code.

To identify cutoff fidelity values for labelling a qubit faulty, we need to compare the logical performance when we keep the faulty qubits against the results from disabling them.

We use the stability experiment [15] instead of the more standard memory experiment that we used in the previous

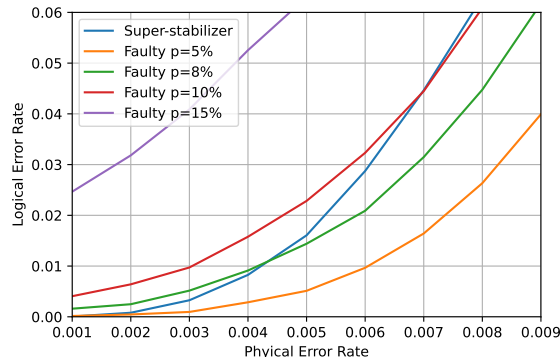


Figure 20: Stability experiment results from keeping/disabling a bad data qubit on a $d = 5$ surface code. The x-axis is the physical error rate of the good qubits.

sections. While the memory experiment quantifies how well a logical observable is maintained by the code, the stability experiment evaluates how well a logical observable can be moved (a capacity that is needed for logical operations). As explained in [15], measurement errors can't cause logical errors in memory experiments except by creating confusion that hides the key data errors. Since errors caused by a faulty qubit looks like repeated measurement errors, the memory experiment is unable to show the damage of faulty qubits.

In Fig.20 we show the results from a stability experiment where the data qubit in the center of a $d = 5$ surface code has higher error rate than the rest. We set the value of p , the two-qubit error rate of the worse qubit, to values from 5% to 15% (the other errors on it scale accordingly). Then we compare the results against the one from disabling the worse qubit and using super-stabilizers around it. The figure shows that when p of the bad qubit is above $\sim 10\%$, we should disable it regardless of the quality of the other qubits. When p is below 5%, it is preferable to keep it unless the error rate on the other qubits is below the range in the plot. And when $p = 8\%$, we should disable the qubit if the error rate on the other qubits is below $\sim 0.45\%$.

6. Related work

The work of Auger et al. [2] consider arbitrary defects for the unrotated surface code, which uses $\sim 2X$ more physical qubits per logical qubit for a commensurate code distance with the rotated code. Moreover, as the authors point out, it is not clear if their measurement schedule to read out super-stabilizers will give rise to a threshold. Our simulator includes a new algorithm for deforming boundaries due to the more complicated boundary of rotated surface code. Another difference is, we implement the shells proposed in [35] to mitigate clustered defects.

Some other methods have also been proposed to handle faulty qubits. Nagayama et al. [28] also formed large stabilizers around the defects. They use SWAP gates to collect all

the syndrome information onto one qubit while we adopt the approach that takes the product of gauge operators. Wu et al. [41] developed an algorithm to adapt surface code to devices with sparse connectivity such as the current IBM devices. According to our correspondence with them, their method is more suitable for highly symmetric lattices and is less suitable for handling arbitrary defect distributions.

We focus on static defects in this paper, but transient events such as cosmic rays could result in temporary defects. There are some strategies [37] that are specifically designed for transient defects on QEC code. Ref. [31] recently considered producing shells around large clusters of transiently defective qubits introduced by cosmic rays. This work identifies the importance of varying the schedule of super-stabilizer measurements for clustered defects.

7. Conclusion

Building a large device with modular chiplets provides the flexibility to throw away unwanted chiplets and arrange the rest. Such flexibility is crucial for scaling up quantum devices to support QEC in the presence of fabrication defects. In this work, we implement an automated method to adapt rotated surface code to a defective grid and generate syndrome measurement circuits. Then we run numerical simulations to identify effective indicators for assessing the performance of defective chiplets relative to defect-free chiplets. With these indicators, we evaluate the resource overhead of implementing an array of logical qubits with different target fidelity and under different defect rates. We also analyze how the overhead is affected by factors like the chiplet size.

We have focused on the design that allocates one patch of surface code on each chiplet. Dividing each patch onto multiple chiplets would increase the flexibility in post-selection. However, since inter-chip links are currently $\sim 3X$ worse than on-chip links [32], this decision might increase the logical error rates. Whether further division of chiplets can reduce the overhead could be an interesting subject for future work.

8. Acknowledgements

This work is funded in part by EPiQC, an NSF Expedition in Computing, under award CCF-1730449; in part by STAQ under award NSF Phy-1818914; in part by the US Department of Energy Office of Advanced Scientific Computing Research, Accelerated Research for Quantum Computing Program; and in part by the NSF Quantum Leap Challenge Institute for Hybrid Quantum Architectures and Networks (NSF Award 2016136) and in part based upon work supported by the U.S. Department of Energy, Office of Science, National Quantum Information Science Research Centers. This work was completed in part with resources provided by the University of Chicago's Research Computing Center. FTC is Chief Scientist for Quantum Software at Infleqtion and an advisor to Quantum Circuits, Inc. BJB is grateful for the hospitality of the Center for Quantum Devices at the University of Copenhagen.

References

- [1] Rajeev Acharya, Igor Aleiner, Richard Allen, Trond I. Andersen, Markus Ansmann, Frank Arute, Kunal Arya, Abraham Asfaw, Juan Atalaya, Ryan Babbush, Dave Bacon, Joseph C. Bardin, Joao Basso, Andreas Bengtsson, Sergio Boixo, Gina Bortoli, Alexandre Bourassa, Jenna Bovaird, Leon Brill, Michael Broughton, Bob B. Buckley, David A. Buell, Tim Burger, Brian Burkett, Nicholas Bushnell, Yu Chen, Zijun Chen, Ben Chiaro, Josh Cogan, Roberto Collins, Paul Conner, William Courtney, Alexander L. Crook, Ben Curtin, Dripto M. Debroy, Alexander Del Toro Barba, Sean Demura, Andrew Dunsworth, Daniel Eppens, Catherine Erickson, Lara Faoro, Edward Farhi, Reza Fatemi, Leslie Flores Burgos, Ebrahim Forati, Austin G. Fowler, Brooks Foxen, William Giang, Craig Gidney, Dar Gilboa, Marissa Giustina, Alejandro Grajales Dau, Jonathan A. Gross, Steve Habegger, Michael C. Hamilton, Matthew P. Harrigan, Sean D. Harrington, Oscar Higgott, Jeremy Hilton, Markus Hoffmann, Sabrina Hong, Trent Huang, Ashley Huff, William J. Huggins, Lev B. Ioffe, Sergei V. Isakov, Justin Iveland, Evan Jeffrey, Zhang Jiang, Cody Jones, Pavol Juhas, Dvir Kafri, Kostyantyn Kechedzhi, Julian Kelly, Tanuj Khattar, Mostafa Khezri, Mária Kieferová, Seon Kim, Alexei Kitaev, Paul V. Klimov, Andrey R. Klots, Alexander N. Korotkov, Fedor Kostritsa, John Mark Kreikebaum, David Landhuis, Pavel Laptev, Kim-Ming Lau, Lily Laws, Joonho Lee, Kenny Lee, Brian J. Lester, Alexander Lill, Wayne Liu, Aditya Locharla, Erik Lucero, Fionn D. Malone, Jeffrey Marshall, Orion Martin, Jarrod R. McClean, Trevor McCourt, Matt McEwen, Anthony Megrant, Bernardo Meurer Costa, Xiao Mi, Kevin C. Miao, Masoud Mohseni, Shirin Montazeri, Alexis Morvan, Emily Mount, Wojciech Mruczkiewicz, Ofer Naaman, Matthew Neeley, Charles Neill, Ani Nersisyan, Hartmut Neven, Michael Newman, Jun How Ng, Anthony Nguyen, Murray Nguyen, Murphy Yuezhen Niu, Thomas E. O'Brien, Alex Opremcak, John Platt, Andre Petukhov, Rebecca Potter, Leonid P. Pryadko, Chris Quintana, Pedram Roushan, Nicholas C. Rubin, Negar Saei, Daniel Sank, Kannan Sankararaman, Kevin J. Satzinger, Henry F. Schurkus, Christopher Schuster, Michael J. Shearn, Aaron Shorter, Vladimir Shvarts, Jindra Skrzyn, Vadim Smelyanskiy, W. Clarke Smith, George Sterling, Doug Strain, Marco Szalay, Alfredo Torres, Guifre Vidal, Benjamin Villalonga, Catherine Vollgraff Heidweiller, Theodore White, Cheng Xing, Z. Jamie Yao, Ping Yeh, Juhwan Yoo, Grayson Young, Adam Zalcman, Yaxing Zhang, Ningfeng Zhu, and Google Quantum AI. Suppressing quantum errors by scaling a surface code logical qubit. *Nature*, 614(7949):676–681, 2023.
- [2] James M Auger, Hussain Anwar, Mercedes Gimeno-Segovia, Thomas M Stace, and Dan E Browne. Fault-tolerance thresholds for the surface code with fabrication errors. *Physical Review A*, 96(4):042316, 2017.
- [3] Michael E Beverland, Benjamin J Brown, Michael J Kastoryano, and Quentin Marolleau. The role of entropy in topological quantum error correction. *Journal of Statistical Mechanics: Theory and Experiment*, 2019(7):073404, 2019.
- [4] H. Bombin and M. A. Martin-Delgado. Topological quantum error correction with optimal encoding rate. *Phys. Rev. A*, 73:062303, Jun 2006.
- [5] Sergey Bravyi and Alexei Kitaev. Universal quantum computation with ideal clifford gates and noisy ancillas. *Phys. Rev. A*, 71:022316, Feb 2005.
- [6] Sergey Bravyi and Alexander Vargo. Simulation of rare events in quantum error correction. *Phys. Rev. A*, 88:062308, Dec 2013.
- [7] Benjamin J. Brown. Conservation laws and quantum error correction: Towards a generalised matching decoder. *IEEE BITS the Information Theory Magazine*, pages 1–12, 2023.
- [8] Benjamin J. Brown, Katharina Laubscher, Markus S. Kesselring, and James R. Wootton. Poking holes and cutting corners to achieve clifford gates with the surface code. *Phys. Rev. X*, 7:021029, May 2017.
- [9] Eric Dennis, Alexei Kitaev, Andrew Landahl, and John Preskill. Topological quantum memory. *Journal of Mathematical Physics*, 43(9):4452–4505, 2002.
- [10] Austin G Fowler and Craig Gidney. Low overhead quantum computation using lattice surgery. *arXiv preprint arXiv:1808.06709*, 2018.
- [11] Austin G Fowler, Matteo Mariantoni, John M Martinis, and Andrew N Cleland. Surface codes: Towards practical large-scale quantum computation. *Physical Review A*, 86(3):032324, 2012.
- [12] Florian N. M. Froning, Leon C. Camenzind, Orson A. H. van der Molen, Ang Li, Erik P. A. M. Bakkers, Dominik M. Zumbühl, and Floris R. Braakman. Ultrafast hole spin qubit with gate-tunable spin-orbit switch functionality. *Nature Nanotechnology*, 16(3):308–312, 2021.
- [13] Jay M Gambetta, Jerry M Chow, and Matthias Steffen. Building logical qubits in a superconducting quantum computing system. *npj Quantum Information*, 3(1):1–7, 2017.
- [14] Craig Gidney. Stim: a fast stabilizer circuit simulator. *Quantum*, 5:497, July 2021.
- [15] Craig Gidney. Stability Experiments: The Overlooked Dual of Memory Experiments. *Quantum*, 6:786, August 2022.
- [16] Craig Gidney and Austin G. Fowler. Efficient magic state factories with a catalyzed $|CCZ\rangle$ to $|T\rangle$ transformation. *Quantum*, 3:135, April 2019.
- [17] Lov K Grover. A fast quantum mechanical algorithm for database search. In *Proceedings of the twenty-eighth annual ACM symposium on Theory of computing*, pages 212–219, 1996.
- [18] Nico W. Hendrickx, William I. L. Lawrie, Maximilian Russ, Floor van Riggelen, Sander L. de Snoo, Raymond N. Schouten, Amir Sammak, Giordano Scappucci, and Menno Veldhorst. A four-qubit germanium quantum processor. *Nature*, 591(7851):580–585, 2021.
- [19] Jared B Hertzberg, Eric J Zhang, Sami Rosenblatt, Easwar Magesan, John A Smolin, Jeng-Bang Yau, Vivekananda P Adiga, Martin Sandberg, Markus Brink, Jerry M Chow, et al. Laser-annealing josephson junctions for yielding scaled-up superconducting quantum processors. *npj Quantum Information*, 7(1):1–8, 2021.
- [20] Oscar Higgott and Craig Gidney. Sparse blossom: correcting a million errors per core second with minimum-weight matching. 2023.
- [21] Clare Horsman, Austin G Fowler, Simon Devitt, and Rodney Van Meter. Surface code quantum computing by lattice surgery. *New Journal of Physics*, 14(12):123011, dec 2012.
- [22] A.Yu. Kitaev. Fault-tolerant quantum computation by anyons. *Annals of Physics*, 303(1):2–30, 2003.
- [23] JM Kreikebaum, KP O'Brien, A Morvan, and I Siddiqi. Improving wafer-scale josephson junction resistance variation in superconducting quantum coherent circuits. *Superconductor Science and Technology*, 33(6):06LT02, 2020.
- [24] Sebastian Krinner, Nathan Lacroix, Ants Remm, Agustin Di Paolo, Elie Genois, Catherine Leroux, Christoph Hellings, Stefania Lazar, Francois Swiadek, Johannes Herrmann, Graham J. Norris, Christian Kraglund Andersen, Markus Müller, Alexandre Blais, Christopher Eichler, and Andreas Wallraff. Realizing repeated quantum error correction in a distance-three surface code. *Nature*, 605(7911):669–674, 2022.
- [25] Daniel Litinski. A Game of Surface Codes: Large-Scale Quantum Computing with Lattice Surgery. *Quantum*, 3:128, March 2019.
- [26] Matt McEwen, Dvir Kafri, Z Chen, Juan Atalaya, KJ Satzinger, Chris Quintana, Paul Victor Klimov, Daniel Sank, C Gidney, AG Fowler, et al. Removing leakage-induced correlated errors in superconducting quantum error correction. *Nature communications*, 12(1):1761, 2021.
- [27] Clemens Müller, Jared H Cole, and Jürgen Lisenfeld. Towards understanding two-level-systems in amorphous solids: insights from quantum circuits. *Reports on Progress in Physics*, 82(12):124501, 2019.
- [28] Shota Nagayama, Austin G Fowler, Dominic Horsman, Simon J Devitt, and Rodney Van Meter. Surface code error correction on a defective lattice. *New Journal of Physics*, 19(2):023050, 2017.
- [29] Joe O'Gorman and Earl T Campbell. Quantum computation with realistic magic-state factories. *Physical Review A*, 95(3):032338, 2017.
- [30] Peter W Shor. Polynomial-time algorithms for prime factorization and discrete logarithms on a quantum computer. *SIAM review*, 41(2):303–332, 1999.
- [31] Adam Siegel, Armands Strikis, Thomas Flatters, and Simon Benjamin. Adaptive surface code for quantum error correction in the presence of temporary or permanent defects. *arXiv preprint arXiv:2211.08468*, 2022.
- [32] Kaitlin N Smith, Gokul Subramanian Ravi, Jonathan M Baker, and Frederic T Chong. Scaling superconducting quantum computers with chiplet architectures. In *2022 55th IEEE/ACM International Symposium on Microarchitecture (MICRO)*, pages 1092–1109. IEEE, 2022.
- [33] Thomas M. Stace and Sean D. Barrett. Error correction and degeneracy in surface codes suffering loss. *Phys. Rev. A*, 81:022317, Feb 2010.
- [34] Thomas M. Stace, Sean D. Barrett, and Andrew C. Doherty. Thresholds for topological codes in the presence of loss. *Phys. Rev. Lett.*, 102:200501, May 2009.
- [35] Armands Strikis, Simon C Benjamin, and Benjamin J Brown. Quantum computing is scalable on a planar array of qubits with fabrication defects. *arXiv preprint arXiv:2111.06432*, 2021.

- [36] Neereja Sundaresan, Theodore J. Yoder, Youngseok Kim, Muyuan Li, Edward H. Chen, Grace Harper, Ted Thorbeck, Andrew W. Cross, Antonio D. Córcoles, and Maika Takita. Matching and maximum likelihood decoding of a multi-round subsystem quantum error correction experiment, 2022.
- [37] Yasunari Suzuki, Takanori Sugiyama, Tomochika Arai, Wang Liao, Koji Inoue, and Teruo Tanimoto. Q3de: A fault-tolerant quantum computer architecture for multi-bit burst errors by cosmic rays. In *2022 55th IEEE/ACM International Symposium on Microarchitecture (MICRO)*, pages 1110–1125. IEEE, 2022.
- [38] Yu Tomita and Krysta M. Svore. Low-distance surface codes under realistic quantum noise. *Phys. Rev. A*, 90:062320, Dec 2014.
- [39] Chenyang Wang, Jim Harrington, and John Preskill. Confinement-higgs transition in a disordered gauge theory and the accuracy threshold for quantum memory. *Ann. Phys.*, 303:31, 2003.
- [40] Fern H E Watson and Sean D Barrett. Logical error rate scaling of the toric code. *New Journal of Physics*, 16(9):093045, sep 2014.
- [41] Anbang Wu, Gushu Li, Hezi Zhang, Gian Giacomo Guerreschi, Yufei Ding, and Yuan Xie. A synthesis framework for stitching surface code with superconducting quantum devices. In *Proceedings of the 49th Annual International Symposium on Computer Architecture*, pages 337–350, 2022.